Numerical study of stress tensors in Poiseuille flow of suspensions

Athonu Chatterjee and David R. Heine
Corning Incorporated, Corning, New York 14831, USA

(Received 22 April 2010; revised manuscript received 17 June 2010; published 13 August 2010)

In this paper, the flow of dense suspensions of monodisperse spheres in wall-bounded channels is studied using a mesoscopic numerical model based on the dissipative particle dynamics (DPD) technique. Experimental observations [for instance, L. Isa *et al.*, Phys. Rev. Lett. **98**, 198305 (2007)] have confirmed that understanding the relevant physics of this problem requires probing at the mesoscopic level to account for the particle scale behavior. The DPD-based approach presented here enables us to explore various aspects of suspension flow at the particle scale. The yielding behavior of the suspensions is studied using macroscopic stress components calculated from the particle level. The relationship between various normal and shear stress components at the yielding plane is presented and discussed. It is seen that in dense suspensions, yielding is characterized by a strong dependence on all the stress components: τ_{xx}, τ_{xy}, and τ_{yy}. It is also seen that different stress components have different length-scale dependencies. While the normal stress in the flow direction, τ_{xx}, depends on macroscopic parameters such as the driving force, τ_{yy}, the normal stress transverse to the flow, depends on particle level parameters and is independent of the driving force. Wall topologies with characteristic dimensions on the order of the suspension particle size have a strong effect on the flow characteristics and the stress components.

DOI: 10.1103/PhysRevE.82.021401 PACS number(s): 82.70.Dd, 82.70.Kj

I. INTRODUCTION

Dense suspensions with viscous liquids as the solvent and having 50% or more solid loading (by volume) are rightly referred to as complex fluids for their inherent complexities, much of which are not understood. Interactions, both hydrodynamic and nonhydrodynamic (electrostatic), between the constituents spanning several orders of time and length scales result in a complex rheological behavior. When these suspensions flow in a wall-bounded region, these complexities are further magnified [1]. Because of the rigid nature of the walls, hydrodynamic behavior of the suspension near them is different from that in the bulk. This has a strong effect on the rheology of the flowing suspension. Similarly, the material of the wall (which is mostly different from the suspension materials) can introduce a new set of electrostatic interactions with the suspension constituents that can affect the rheology. Wall topology is also seen to have a strong effect on suspension dynamics [1].

The most noticeable effect of a wall on flowing dense suspensions is the structural segregation that takes place in the suspension where solid particles move away from the walls toward the center of the channel. As a consequence, a shear zone is formed near the wall in which a finite velocity gradient or shear exists and a plug zone is formed away from the wall in which macroscopic velocity gradients are zero and the plug moves like a rigid body. Also, there is an apparent wall slip.[1–5]

In Fig. 1 the above are illustrated in a Poiseuille flow type of setup, which will be the model system for all analyses in this work. Typically, these materials are treated as a continuum fluid for the purpose of predicting their behavior in a production environment. The most widely used continuum model is the Herschel-Bulkley (HB) constitutive equation, which treats the material as a Bingham fluid with a predefined yield stress [5]. However, this continuum picture of the suspension fails to describe fully the observed behavior of suspension flow [2,6]. For instance, confocal microscopy imaging techniques by Isa *et al.* [2] have highlighted the limitations of a continuum approach. They observed that the shear layer thickness remains constant over a vast range of the driving force, a behavior that the continuum model cannot explain. Recently, Bonn and Denn in Ref. [6] discuss the limitations of the concept of an invariant stress for yielding behavior. Along the same line, Yan *et al.* [7] recently showed that for a single material HB parameters depend strongly on the extent of flow confinement, further making their use ambiguous. These observations demonstrate that much of the physics associated with suspension flow are particle-level phenomena, and the use of continuum-type description has limitations.

Numerical simulations of wall effects, therefore, have to be able to probe the mesoscopic regime for most systems of interest since the typical particle sizes range from nanometers to microns. In this work, we use a dissipative particle dynamics (DPD)-type scheme. DPD [8–12] is a mesoscopic particle-based technique for simulating fluid behavior that incorporates the hydrodynamic effects in dense suspensions of viscous fluids. With its inherent particle nature, it is well

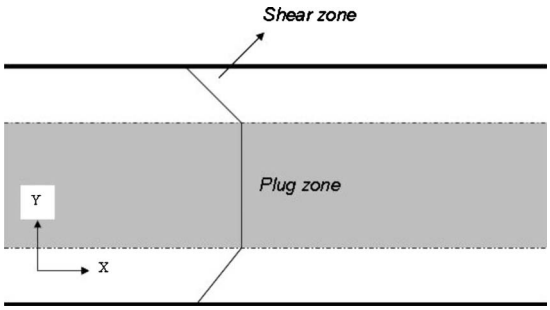

FIG. 1. A simple depiction of wall effects. Also, the model set-up used for analysis in this work. Flow is in the *X* direction.

suited for modeling wall effect problems where there are multiple components in the system. Here, we use the DPD approach to study the yielding phenomenon and the effect of wall topology in highly filled suspensions.

Numerical simulations presented confirm the observations from experiments with regard to shear layer thickness and yielding [2,6]. It is also seen that some stress components depend only on system level parameters like driving force, whereas other stress components depend only on particle level parameters such as wall topology and particle characteristics. Together these stress components paint a complex picture of the yielding phenomenon.

A quantitative study of the effect of wall topology is also presented in this paper. It is seen that wall topology with topological dimensions comparable to the particle size, which is small compared to the overall system dimensions, has a strong effect on flow characteristics.

The remainder of this paper is organized as follows. In Sec. II, the model problem and the numerical technique are described. In Sec. III, the case of planar walls is investigated. Validation with experiments is presented in this section. In Sec. IV, the analysis is extended to nonplanar topologies and Sec. V summarizes this work and presents some concluding comments.

II. MODEL PROBLEM AND THE NUMERICAL TECHNIQUE

A. Model description

The system studied is shown pictorially in Fig. 1. We simulate the flow of a dense suspension of monodisperse spherical particles between two parallel walls under the action of an imposed pressure gradient, which can be closely approximated by a unidirectional body force. We now describe the different particle interactions in the system.

1. Fluid-fluid interaction: DPD thermostat

The fluid is described by fluid particles (or DPD particles) using the standard DPD approach [8–12]. The total force acting on each fluid particle due to neighboring fluid particles is given as

$$f = \sum (F_f^C + F_f^D + F_f^R), \tag{1}$$

where the sum runs over each neighboring particle within a cutoff distance σ. Throughout this paper, we use dimensionless units such that $\sigma=1$, and $\varepsilon=\kappa T=1$ define the units of length and energy, and the mass of the fluid particle $m_f=1$. Nondimensionalization is described in details in Sec. II C. The conservative force between fluid particles is described as a linear potential [9]

$$F_f^C = \begin{cases} a(1-r_f)\hat{r} & r \le 1 \\ 0 & r > 1 \end{cases}, \tag{2}$$

where a is set to $75\kappa T/N$ to match the compressibility of water [9], N being particle number density. As explained in Groot and Warren [9], a value of N of 3 or greater suffices. In this work $N=3$. The dissipative and random forces acting on the fluid particles are

$$F_f^D = -\gamma w^D(r)(\hat{r}\cdot v)\hat{r}, \tag{3}$$

$$F_f^R = \sigma_R \omega^R(r)\theta\hat{r}, \tag{4}$$

where $\gamma=4.5$, $w^D(r)=w^R(r)^2=(1-r)^2$ for $r<1$, v is the relative velocity between the fluid particles, $\sigma_R^2=2\gamma$, and θ is a random number with Gaussian statistics.

The works of Flekkoy *et al.* [10], Groot and Warren [9], Marsh [12], etc., have put DPD on firm theoretical footing. Pivkin and Karniadakis [13] have reported the use of DPD to successfully solve canonical fluid mechanics problem such as Poiseuille flow, Couette flow, etc. DPD has also been used to simulate the rheology of suspensions with success as reported in the works of Hoogerbrugge and Koelman [8], Chatterjee and Wu [11], Boek, *et al.* [14] and Whittle and Dickinson [15]. Our use of DPD in this work is along the same line as the mentioned works and therefore is well validated. Some additional validations specific to the problem on hand are presented later.

2. Solid-solid Interaction

In this work a hard-sphere model of suspension [11,14,15] is used to confirm with the experiments reported in Ref. [2] in which hard-sphere suspensions were used. In such a model, the predominant interaction between the colloids is hydrodynamic interaction, and this is augmented by a weak electric double layer (EDL) repulsion of the form given in Eq. (5) [15,16], primarily for stability purposes.

$$F(h) = F_0 \exp(-\kappa h) \tag{5}$$

h in Eq. (5) is the distance between the solid surfaces. The nondimensionalized values of F_0 and κ used in the simulations are 25 and 5, respectively, for $kT=4\times10^{-21}$ J ($T=300$ K) and a nondimensional length scale, σ, of 5 μm. Please see Sec. II C for details on nondimensionalization. These values correspond to passive (extremely low charge density) spherical polystyrene particles in water (pH$\sim$7). Typical pertinent dimensional values would be [16]: surface charge density=1.5 μC/m^2; zeta potential=2 mV; Debye length=960 nm.

To tackle densely loaded suspensions, a lubrication force is explicitly applied between the solid particles when the surface separation is less than 10% of the solid radius [17]. The center-to-center lubrication force between two spherical particles of radius r_1 and r_2 with the surfaces at a separation of ξ is [17,18]

$$F_{\text{lub}} = -\frac{6\pi\mu r_{red}^2}{\xi} V_{rel} \tag{6}$$

to the order of ξ^{-1} where

$$r_{red} = \frac{r_1 r_2}{r_1 + r_2}. \tag{7}$$

V_{rel} is the relative velocity between the particles, and μ is the viscosity of the solvent. To obtain μ for Eq. (2) in nondimensionalized units, the kinetic expression for DPD shear viscosity [12] is used, which for the DPD parameters used here boils down to

$$\mu = \frac{2\pi n^2 \gamma}{1575} + \frac{45}{4\pi\gamma}, \tag{8}$$

where $n=3$ is the DPD fluid particle density. The R.H.S. of Eq. (6) has a singularity at $\xi=0$ and therefore below a lower bound of separation its value is kept fixed at the value at the lower bound. This lower bound is chosen to be 1% of the cutoff radius.

3. Solid-fluid interaction

As noted in the works of Whittle and Dickinson [15] and later validated with experiments by Chatterjee and Wu [11], and Chatterjee *et al.* [19], the spherical shape of the solid particles allows the use of DPD-type interaction between the solid and fluid particles. The cutoff distance, σ, for the forces now are taken from the solid surface, meaning, the effective cutoff distance from the center increases to account for the finite volume of the colloid. For the conservative force [Eq. (2)], a value of a of around $a_{ff}/2$ was found to be appropriate [15]; a_{ff} being the fluid-fluid counterpart. For the coefficient of dissipative force, γ, long-term simulations showed that the fluid-fluid value of 4.5 was appropriate [11,15], and this value was used in the present simulations.

B. Modeling the wall

A wall is represented as a frozen collection of DPD fluid particles that can be arranged in any topology [3,8,11,13,14]. In Fig. 3, examples of a few wall topologies generated by freezing spherical particles are shown. Interaction between wall particles and the particles constituting the suspension demand close attention in light of this approximate representation. Impenetrability and hydrodynamic no-slip behavior with the fluid should be satisfied by this interaction [13]. Also, nonhydrodynamic interactions, if any, between the wall particles and the solid particles in the suspension should be accounted for.

In this work, the basic conditions of impenetrability and hydrodynamic no-slip with the fluid are implemented using the DPD force parameters suggested by Pivkin and Karniadakis [13]. Based on their analysis, in which essentially a force balance is conducted on a fluid particle near the wall, the conservative force parameter, a, is equal to 9.01 [Eq. (1)], for the wall and fluid particle interaction. Readers are referred to their work [13] for details. Between the wall and solid particles, a lubrication force is applied at close proximity as explained above. Despite the application of these interactions, some suspension particles do escape from the domain because of the soft nature of the interactions. A bounce-back condition is employed [11,13] to put these particles back into the domain. In a bounce-back operation the escaped particles are placed back into the domain with the relative velocity between the particle and the wall reversed. Since the wall is stationary, the velocity of the particle is reversed.

The above mentioned wall treatment was extended to nonplanar walls of topologies shown in Figs. 2 and 3 and the bounce-back condition was adapted to the nonplanar nature of the wall. To conveniently do so in a tractable manner, the escaped particles are placed into the domain with their Cartesian velocity components reversed in sign. Since the wall particles are stationary, essentially this means that the relative velocity between the particle and wall is reversed. These operations in conjunction with well-monitored time steps and DPD thermostat performance ensures the fidelity of wall treatment. Our experience has shown that if bounce-back condition is not applied properly or if there are too many of them (because of large time-step value or faulty interactions) the DPD thermostat, which is required to maintain a value of kT close to 1, doesn't function properly. This criterion ensures proper functioning of this operation.

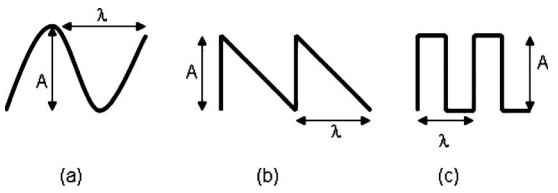

FIG. 2. The wall topologies considered in this work are: (a) sinusoid, (b) sawtooth, and (c) square. "A" represents the roughness amplitude and "λ" the wavelength.

We consider three periodic topologies for these nonplanar walls: sinusoid, sawtooth and square well, as shown in Figs. 2 and 3. The characteristic dimensions of these topologies, amplitude (A) and wavelength (λ), are of the same order of magnitude as the size of the solid particle in the suspension, $A=2\sigma_c$ and $\lambda=2\sigma_c$ or $4\sigma_c$, where σ_c is the radius of the solid particle.

C. Model implementation

Referring to Fig. 1, the flow direction (the direction of the imposed driving force) is the x direction and the walls are in the y direction. Periodic boundary conditions are imposed in the x and z directions. Walls are explicitly treated in the manner described in Sec. II B. The pressure gradient, which is the driving force, is implemented by applying a constant body force on the fluid particles [13,21]. This force is re-

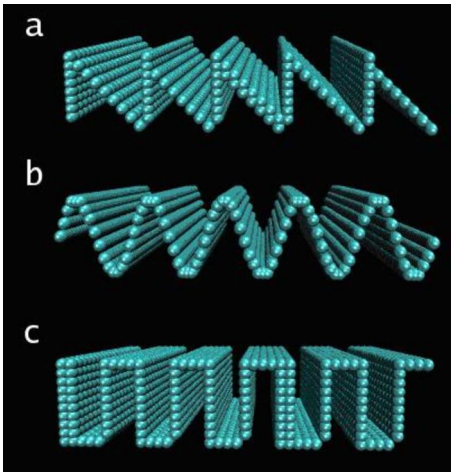

FIG. 3. (Color online) Rendition of nonplanar walls used in the simulations: (a) sawtooth, (b) sine, and (c) square well geometries.

ferred to in the text interchangeably as driving force or imposed pressure gradient and is represented by the symbol F_D. The systems modeled here typically have low mean velocities that are unidirectional along the axis of the channel at steady state. Also, the ratio of the length of the channel to the width is very high. For such systems the pressure gradient along the axis can be approximated by applying a constant body force. Simulations are run long enough to ensure that steady bulk velocity profiles are reached and the system is then analyzed.

As mentioned earlier, a standard nondimensionalization procedure [9] is used in which the nondimensionalization parameters are: the cutoff radius σ for length, mass of the DPD fluid particle for mass, and kT for energy. The value of nondimensional colloid radius, σ_c (the ratio of the radius of the solid particle to the cutoff radius) has important implications as it determines the hydrodynamic length scales being resolved (or ignored). The larger the value of this radius, smaller the length scales resolved, but then one needs larger domain size, which results in more computations! Following the analysis presented in Padding and Louis [20], in this work we used a value of 1.25 for nondimensional colloid radius (σ_c), or 2.5 for colloid diameter, which was found to be an optimal balance.

To get a sense of real dimensions we are talking about here, if σ (cutoff radius) is chosen to be 5 μm (a typical mesoscopic value), then the colloid diameter (2.5σ) is 12.5 microns. Based on particle number density value of 3 for fluid particles, the radius of a fluid particle is about 0.4σ (2 μm). As mentioned below in Sec. III A, the channel width used in this study is 50σ and therefore has a value of 25 or 0.25 mm. This width to particle size ratio was chosen to mimic reality in typical extrusion processes [5]. Also, a similar channel width was used in the experiments reported in Ref. [2], which is used to validate the numerical model.

To get an idea of dimensional values of velocities, as explained in Padding and Louis [20] and also in Chatterjee *et al.* [19], one has to equate the Peclet number ($Pe=6\pi\mu a^3\gamma_w/kT$) for the coarse-grained model system and the real system in order to capture the ratio of diffusive time scale to Stokes time scale. γ_w in Peclet number definition for this problem could be taken as shear rate at the wall or the wall shear stress divided by viscosity. Using the viscosity of water at $T=300$ K of 10^{-3} Pa s, a typical nondimensional wall shear stress of 1 (see Fig. 11 for instance) and other dimensional and nondimensional values of colloid radius noted above, one can estimate a dimensional shear rate of around 0.3 sec^{-1} at the wall for this system. For the sake of obtaining approximate values, if one considers the velocity to be linear in the shear layer (see Fig. 5 for reference) and the shear layer thickness is seven times the colloid diameter, then the velocity differential across the shear layer is around 25 μm/s. Note that these are typical values just to give an estimate.

In this work, the simulations were performed using large-scale atomic/molecular massively parallel simulator (LAMMPS), a multiscale, particle-level solver [22]. Long-time simulations are performed to ensure converged solutions. Convergence is gauged by monitoring the bin-averaged quantities (see below). Typical time-step values used range from 10^{-3} for lower driving forces to 10^{-4} for higher driving forces. Typically, total number of time-steps simulated lie between 5 and 15 millions. The parallel-computing capacity of LAMMPS enabled the use of multiple processors to speed up the simulations. The use of LAMMPS for analyzing shear rheology of suspensions with explicit solvent has also been reported in Refs. [23,24]. The systems simulated here typically have 400–1200 colloidal particles and 8000–15,000 fluid particles depending on the geometry and solid loading. These numbers come from system size and the particle sizes. For instance, for a computational domain of volume V (=7200 in this work for planar wall cases), for a suspension of 50% loading with a fluid particle density of 3, the number of fluid particles will be $0.5\times V\times 3=10\,800$. Using a similar logic, the number of colloid particles of radius 1.25 will be around 450.

Bin-averaged quantities are used to assess the macroscopic behavior of the system. These quantities are averaged over 2 million time-steps and the spatial extent of the bins. The bins span across the length of the channel in the x direction and have a thickness of $2\sigma_c$ (colloid diameter). The bin number increases from the lower wall ($y=0$) to the upper wall. Because the walls, which are frozen aggregates of spherical particles, have a finite thickness, the averaged values at the first and the last bins are ignored throughout this work. Simulation results measured at the wall are taken from the second and the second-last bins in the system [3].

Fluctuational quantities are significant in dense suspension flows [2,25] and they need to be quantified appropriately. In this work, shear stress fluctuations in the shear layer near the wall are used to validate the numerical method with experiments. The stress components themselves are calculated from the inter-particle interactions as described in Ref. [26]. The fluctuations of the stress components, $\Delta\tau_{\alpha\beta}$, are calculated using:

$$\overline{\langle\Delta\tau_{\alpha\beta}^2\rangle}=\overline{\langle\tau_{\alpha\beta}^2\rangle}-\overline{\langle\tau_{\alpha\beta}\rangle}^2, \tag{9}$$

where $\tau_{\alpha\beta}$ is the $\alpha\beta$ component of the stress tensor, angular brackets indicate stress averaging and the overbar indicates time averaging. Only $\Delta\tau_{xy}$ was monitored in this work, which is the shear stress component in the xy plane.

III. FLOW IN CHANNELS WITH PLANAR WALLS

A. Facts and validation

We first consider monodisperse suspensions between planar walls to elucidate some fundamental aspects of suspension flow and validate the numerical scheme with the available experimental data. Spherical DPD particles are frozen along the planar y boundaries to mimic the rigid walls (Fig. 3). The distance between the walls is about twenty times the diameter of the solid particles or 50σ. Lengths in x and z periodic directions are 12σ.

In Fig. 4, bin-averaged velocity profiles across the channel (in the y direction) for 60% suspension are presented for different driving forces. As is the case with suspension flows, a plug-type profile is seen in all the cases with a finite slip velocity at the wall.

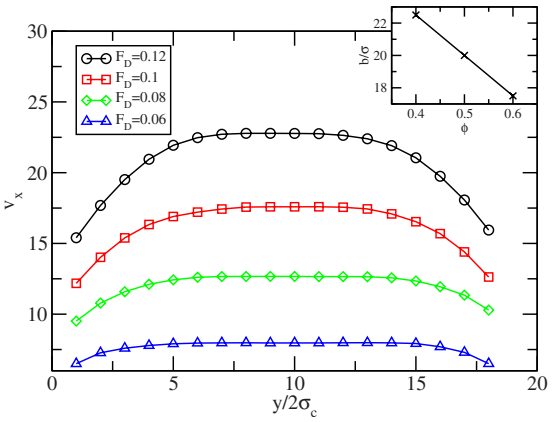

FIG. 4. (Color online) Averaged velocities (V_x) across the channel for 60% suspension and planar walls. Inset: Nondimensionalized shear layer thickness, b/σ, plotted as a function of the solid loading (φ) for three different solid loadings. F_D is the driving force.

The shear layer thickness is quantified as the distance in the y direction from the wall at which the bin-averaged velocity, v, is

$$v = v_S + 0.95(v_c - v_s), \tag{10}$$

where v_s is the slip velocity at the wall and v_c is the velocity of the central core. Based on this, we can see that the shear-layer thickness is independent of the driving-force and is close to $14\sigma_c$ (or 7 times the colloid diameter) for the four driving forces. This is in agreement with the experimental observation of Isa *et al.* [2], and also Pouliquen and Gutfraind [25] for granular suspensions. In the inset of Fig. 4, shear layer is plotted for three different solid loadings. This thickness is independent of the driving force and it increases with a reduction in solid loading.

Isa *et al.* [2] report that the normalized velocity profiles across the channel, defined as $(v-v_s)/(v_c-v_s)$, are identical for different driving forces. The normalized velocities from our simulations of the suspension at 60% loading are plotted in Fig. 5. Here, we see that the normalized velocity profiles are close for the two highest driving forces, but some deviation is observed for the lowest two driving forces. However,

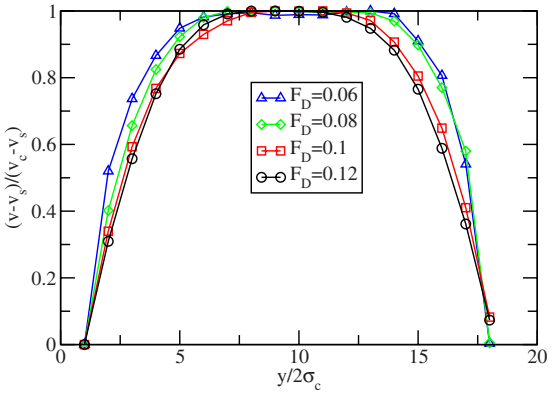

FIG. 5. (Color online) Normalized velocity profiles of Fig. 4 (60% suspension, planar walls). F_D is the driving force.

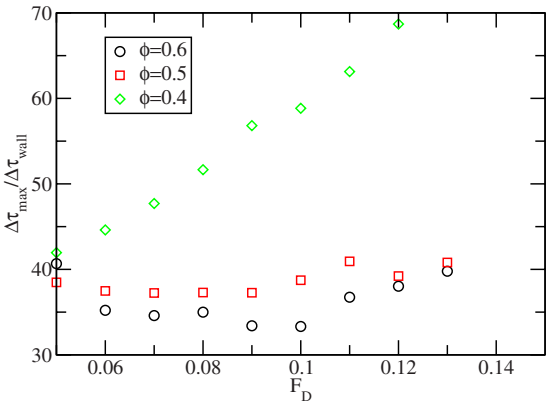

FIG. 6. (Color online) The ratio of the maximum fluctuation of shear stress in the shear layer to the wall shear stress at different driving forces, F_D (planar wall). φ is the solid loading.

each profile shows a central plug with nearly the same shear layer thickness.

Another interesting observation reported by Isa *et al.* [2] is that the amplitude of the stress fluctuations in the shear layer scales almost linearly with the wall shear stress and the ratio between the two is independent of macroscopic quantities such as the driving force. We calculate the average stress fluctuation in each bin for the present simulations using Eq. (9). In Fig. 6 the ratio of the maximum value of fluctuational shear stress in the shear layer (which is in the vicinity of the wall) to the wall shear stress is plotted against driving force for three different solid loadings, 40%, 50%, and 60%. It can be seen that this ratio remains essentially constant for the denser loading values of 50% and 60% while the external driving force increases nearly threefold. For the 40% case, a linear increase in the ratio is seen, possible because it is not dense any more.

To further validate this modeling approach and demonstrate its strength, the macroscopic rheological behavior of the suspension in the shear layer is extracted for 50% and 60% suspensions. Note that in the shear layer the suspension behaves like a viscous fluid. Using the spatial bin-averaged velocity profile (Fig. 4) one can estimate the shear rate $(\partial v/\partial y)$ and relate it with the calculated shear stress to obtain a constitutive relationship. This is shown is Figs. 7 and 8 for 50% and 60% suspensions, respectively. As can be seen, a power-law relationship indeed exists for both the suspension. For the 50% case the index is 0.67 and for the 60% case it is 0.3. This trend is qualitatively correct because as the loading reduces one would expect the system to behave closer to the Newtonian case in which the index is close to 1 (a linear relationship).

B. Analysis of the stress components

The behavior of macroscopic stress components is now examined in greater detail to shed more light on the rheological behavior of the suspension. In Fig. 9, τ_{xx} is plotted across the channel for three different driving forces (0.08, 0.1, and 0.12) for the 60% suspension. It is seen that τ_{xx} is compressive in nature, its magnitude increases with the driv-

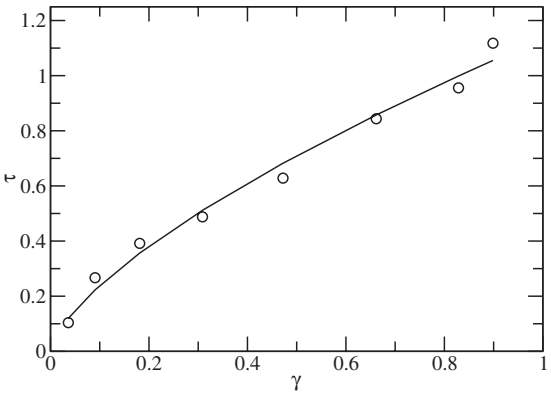

FIG. 7. Plot of shear stress (τ) versus shear rate ($\dot{\gamma}$) in the shear layer of a 50% suspension. A power-law dependence is seen with an index of 0.67. R^2 for this fit is 0.9824.

ing force, and that its magnitude increases in the shear layer and almost plateaus in the central core where plug flow occurs. In Fig. 10, the greatest magnitude of τ_{xx} (which is in the plug zone) is plotted as a function of the central plug velocity for 40%, 50%, and 60% suspensions. For all of these cases, the dependence of τ_{xx} is parabolic with respect to the plug velocity. This relationship, which to our knowledge has not been reported elsewhere, could potentially be an important design consideration for dense suspension flows such as the relationship between shear stress and plug velocity described next.

A plot of shear stress, τ_{xy}, across the channel for different driving forces is shown in Fig. 11 for the 60% suspension. The distribution is linear between the walls, similar to the distribution one would find in a simple Poiseuille flow of liquids, with the highest stress magnitude at the walls. The wall shear stress, which is a parameter of interest in many practical applications, increases linearly with the plug velocity as shown in Fig. 12. This observation is in line with the empirically derived constitutive model, the Benbow—Bridgewater model [1,5]. This model describes the wall shear stress as $\tau_w = \beta v^n$ where n is often close to 1.

However, the behavior of the transverse, normal stress component, τ_{yy}, is different. The variation of τ_{yy} across the channel for different driving forces is plotted in Fig. 13. This

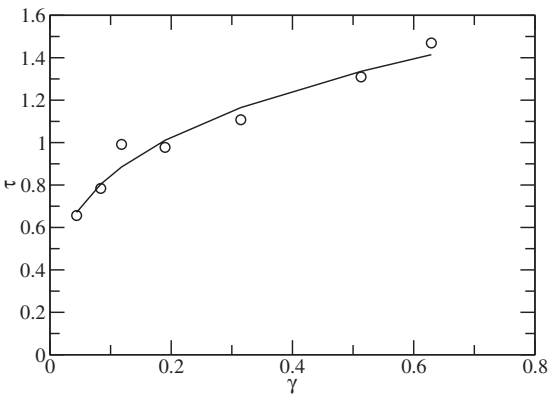

FIG. 8. Plot of shear stress (τ) versus shear rate ($\dot{\gamma}$) in the shear layer of a 60% suspension. A power-law dependence is seen with an index of 0.3. R^2 for this fit is 0.9582.

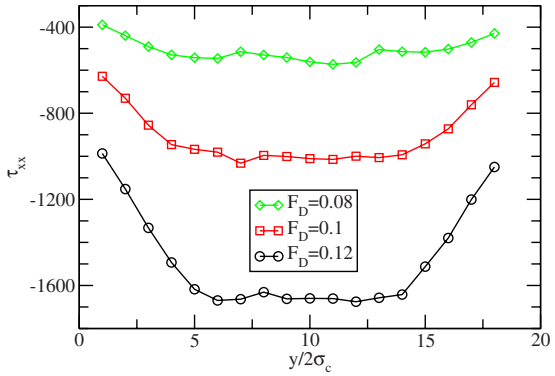

FIG. 9. (Color online) Variation of τ_{xx} across the channel for different driving forces (60% suspension, planar walls). F_D is the driving force

shows that τ_{yy} is independent of the driving force (unlike τ_{xx} and τ_{xy}). As shown in the plot, the magnitude of τ_{yy}, particularly in the central plug region, is roughly the same for all driving forces, in sharp contrast to the behavior of τ_{xx}. The negative value of τ_{yy} throughout indicates that the suspension undergoes compaction perpendicular to the flow direction. This is due to the fact that particles migrate away from the wall and hence the suspension is in a compressed state in the y direction. It is this tendency of compaction that leads to the formation of a central plug region in which the suspension behaves like a rigid body. This region can also be viewed to be in a jammed state, and therefore the whole phenomenon of formation of a plug in the center and shear layer adjacent to the wall can be viewed as an exercise of jamming and unjamming in dense suspensions [6,27–29].

The magnitude of τ_{yy}, however, changes considerably with solid loading as shown in Fig. 14 in which τ_{yy} across the channel is plotted for three different solid loadings (60%, 50%, and 40%) for a driving force of 0.12. This observation indicates that while τ_{xx} and τ_{xy} depend on macroscopic parameters such as the driving force, τ_{yy} does not and it depends on particle level parameters such as the solid concentration, which determines the average distance between the particles and hence the interaction. Later, this point will be

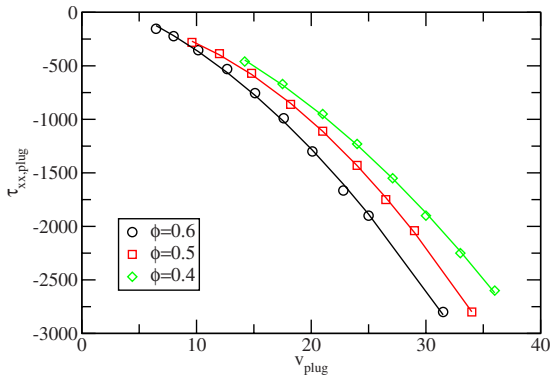

FIG. 10. (Color online) Variation of the magnitude of τ_{xx} in the plug with respect to the plug velocity (planar wall). The symbols are numerically calculated data and the lines are parabolic fits. φ is the solid loading.

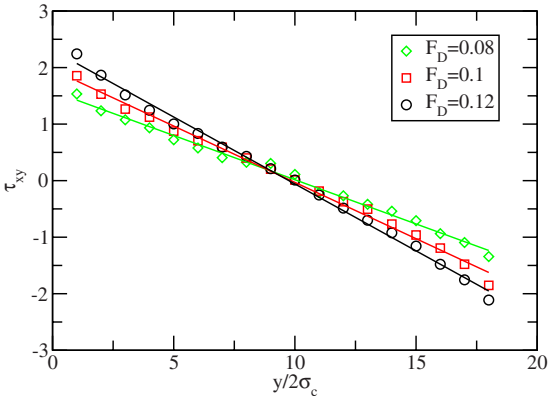

FIG. 11. (Color online) Variation of τ_{xy} across the channel for different driving forces (60% suspension, planar walls). The symbols are numerical data and the lines are linear fits. F_D is the driving force

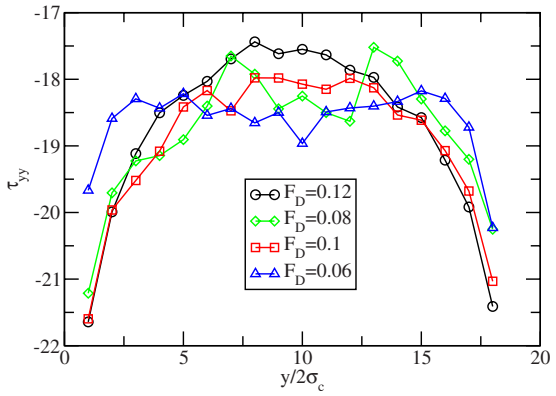

FIG. 13. (Color online) Variation of τ_{yy} across the channel for different driving forces for a 60% suspension with planar walls. F_D is the driving force.

further explained in the context of wall topology. Further, the magnitude of τ_{yy} increases with solid loading, indicating more tendency to jam at higher loadings. In Fig. 4 it was seen that the shear layer thickness decreases with an increase in solid loading and, such as τ_{yy}, is independent of the driving force. These links will be further examined below in the context of yielding.

C. Multidimensional yield surface

The multidimensional nature of yielding in terms of the stress components can now be understood using this analysis. For a suspension, the magnitude of τ_{yy} remains fairly independent of the external driving force. But, the magnitude of wall shear stress increases with the driving force. If shear stress is the sole criterion for yielding (as is the case in most of continuum yield stress formulations), then based on this observation the thickness of the shear layer should increase with the driving force, which is not the case. The reason is that yielding in these suspensions does not depend solely on shear stress; rather it is determined by a multitude of parameters as explained below.

At the edge of the shear layer where yielding takes place, while τ_{xy} increases with the driving force, the magnitude of the compressive τ_{xx} also increases, making the suspension harder to shear. Thus, the effect of increase in τ_{xy} is offset by the increase in the compressive value of τ_{xx}. This behavior maintains the lack of variation of shear layer thickness with respect to the external driving force as seen in the experiments in Ref. [2]. These observations can now be further examined in the manner described below.

For each suspension, flow simulations were performed for different driving forces ranging from 0.05 to 0.14. For each driving force, the values of the stress components at the edge of the shear layer (the yielding plane) given by the criterion described in Eq. (10) were collected. Using these "yield points" for different driving forces, a yielding surface for the suspension is arrived at in the form of a function, $F(\tau_{xx}, \tau_{xy}, \tau_{yy})=0$.

The yield surfaces for the three suspensions (40%, 50%, and 60%) are presented in Table I. It is noteworthy that all three of them are τ_{yy}=constant planes with their magnitudes increasing with the loading. Also the form of the τ_{xx}-τ_{xy} dependence is parabolic in all the cases, also shown pictorially in Fig. 15 for the three suspensions. In essence, the yield planes for the three solid loadings are parallel τ_{yy} planes,

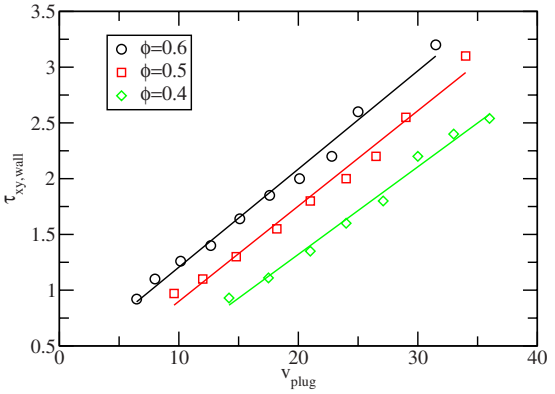

FIG. 12. (Color online) Wall shear stress plotted as a function of plug velocity (planar walls). The symbols are numerical data points and the lines are linear fits.

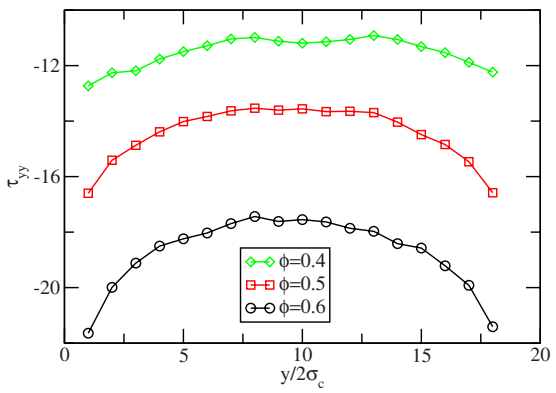

FIG. 14. (Color online) Variation of τ_{yy} across the channel at different volume fractions with planar walls and a driving force F_D=0.12. φ is the solid loading value.

TABLE I. Yield surfaces for different solid volume fractions.

Suspension	Yield surface; $F(\tau_{xx},\tau_{xy},\tau_{yy})=0$
60% loading	$\tau_{xx}=-6759\tau_{xy}^2+2421\tau_{xy}-306$
	$\tau_{yy}=-18$
50% loading	$\tau_{xx}=-2070\tau_{xy}^2-4375\tau_{xy}+677$
	$\tau_{yy}=-13.5$
40% loading	$\tau_{xx}=-15911\tau_{xy}^2-7073\tau_{xy}+313$
	$\tau_{yy}=-11$

indicating that this stress component is decoupled from the other two components that are coupled to each other. This makes sense in light of the fact that τ_{yy} has a particle-level dependence and τ_{xx} and τ_{xy} are dependent on system-level properties. τ_{yy}, it should be noted, pertains to the dilatant behavior of the flowing suspension. It is a measure of the Reynolds dilatancy in the shear layer. The close affinity between yielding and the dilatancy in dense suspensions has also been reported in the experimental work of Fall *et al.* [28].

From Table I and the corresponding figure, Fig. 15, the following insights are obtained about the yielding phenomenon:

(1) The minimum value of τ_{xy} at which yielding takes place increases with solid loading, which is quite intuitive.

(2) On the yield plane, τ_{xx} and τ_{xy} have a parabolic dependence, particularly for the denser cases, 50% and 60%. The trend of this dependence with respect to solid loading shows that as the suspension becomes more dilute, the window of τ_{xy} on the yield plane narrows.

(3) The above point indicates that the singular, shear-stress-based criterion for yielding used in bulk, continuum formulations has limited validity for dilute suspensions. For dense suspensions, as can be seen for the 50% and 60% cases, such a criterion does not hold at all.

(4) Finally, yielding in dense suspensions is intimately related to the dilaltant behavior.

IV. FLOW IN CHANNELS WITH NONPLANAR WALLS—EFFECT OF WALL TOPOLOGY

It has been observed that mesoscopic topological features of the wall have a strong effect on suspension and granular flow [2,25]. Using the numerical technique presented here, simulations incorporating the three wall topologies shown in Fig. 2 have been performed. In Table II, the plug velocities are listed for the planar and nonplanar cases for the 60% suspension for different driving forces. As can be seen, there is a substantial retardation of flow in the nonplanar systems relative to the planar case by a factor of 3.7 on average. Even among the nonplanar walls, the wall topology itself has an appreciable effect on the flow. This is seen in Fig. 16 where the mean velocity profile is plotted across the channel for the three topologies. There is an appreciable difference in the plug velocities in sinusoidal channels compared to square well and sawtooth channels. This is also seen in Table II. The sinusoidal topology yields the lowest velocities. The dependence of plug velocity on topology becomes clearer once the behavior of stress components is studied.

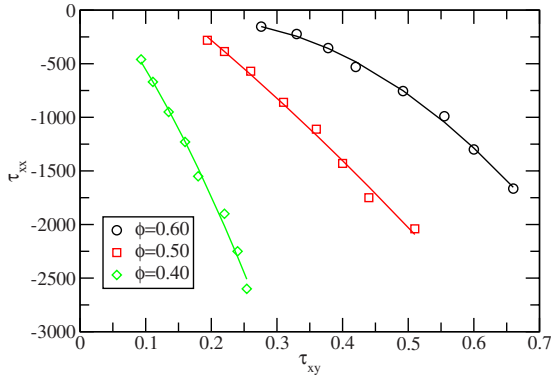

FIG. 15. (Color online) τ_{xx} and τ_{xy} at the yield plane of the suspensions for three volume fractions. φ is the solid loading.

TABLE II. Maximum values of τ_{yy} and plug velocity for a 60% suspension with various wall topologies having $\lambda=2\sigma_c$.

τ_{yy} (Average across the channel)				
	Plane	Sawtooth	Square	Sinusoid
$F_D=0.08$	18	21.4	21.8	24.8
$F_D=0.1$	18	21.7	21.9	25.1
$F_D=0.12$	18	20.8	21.6	25.1
Plug velocity				
	Plane	Sawtooth	Square	Sinusoid
$F_D=0.08$	12.5	2.6	2.8	1.8
$F_D=0.1$	17.6	6	6.2	5.2
$F_D=0.12$	22.7	8.5	8.7	6.5

In Table II, the magnitudes of the maximum values of τ_{yy} and the central plug velocities are listed for different wall topologies for three different driving forces for the 60% suspension. The stress component τ_{yy}, which is a measure of compaction in the direction normal to the flow, shows appreciable dependence on wall topology while it is independent of the driving force. Wall topology is a particle-level param-

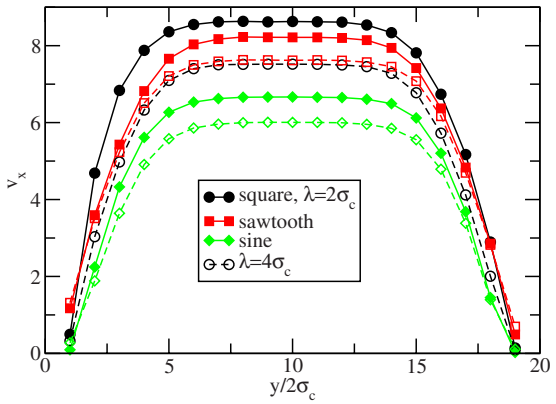

FIG. 16. (Color online) Averaged velocity profiles across the channel for different wall topologies and wavelengths for a 60% suspension with $F_D=0.12$. All closed (filled) symbols are for $\lambda=2\sigma_c$ and open symbols for $\lambda=4\sigma_c$.

eter and this observation reinforces the particle-scale nature of τ_{yy}. The magnitude of τ_{yy} is the highest for the sinusoidal case and the lowest for the planar wall case. The magnitudes of the plug velocities, on the other hand, are in the reverse order. This can be explained as follows. During the flow of suspension, there takes place a competition between flow in the sheared direction and compaction (or dilation) [30]. τ_{yy} is the measure of compaction whereas the plug velocity indicates the flowing ability of the suspension through the channel. The magnitude of τ_{yy} is the highest for the sinusoidal wall indicating that of the four topologies this one gives rise to the highest compaction, and hence it has the lowest plug velocity.

An important conclusion from this result is that in practical applications involving flow of dense suspensions through narrow channels, particle-level parameters such as wall topology play an important role in making the paste more amenable to flow. Intuition often restricts options to macroscopic parameters such as driving force, channel width, etc.

To study the role of the wall topology wavelength, it was increased from $2\sigma_c$ to $4\sigma_c$, and flow simulations were carried out for the 60% suspension to see the effect of this change. For all topologies, a reduction in the plug velocity is seen as the wavelength is increased, as shown in Fig. 16. The reduction lies between 10%–15% again indicating that a small change in wall topology has a noticeable effect on plug velocity. Also, the sinusoidal topology yields the lowest plug velocity, which hasn't been hitherto observed.

V. CONCLUSIONS

In this paper, a modeling strategy was presented to study the flow and deformation of dense suspensions in wall-bounded channels. The study was restricted to suspensions of monodisperse spheres; extension to polydisperse systems is currently underway. A hard-sphere suspension was modeled wherein the standard DPD thermostat was used to resolve the hydrodynamics of the solvent and a weak EDL repulsive force was used for nonhydrodynamic interaction between the solid particles. Since dense suspensions were considered, a lubrication force was applied between the solid particles at close proximity. The modeling approach was qualitatively validated with experimental work on suspension flow in channels [2].

First, the particle nature of the rheology of dense suspension was firmly established. This has been reported in many experimental papers on granular systems [25] and suspensions [2]. By using the capability of this model to identify the yield plane and calculate macroscopic stress components, a multivariate account of yielding with respect to the stress components was established for suspensions of different loadings (Table I and Fig. 15). In line with the experimental findings [2] and other suggestions [6,28,29], it was established that yielding of dense suspensions depends on multiple parameters (stress components in this case) that can be best explained by a yielding surface or a phase diagram [29] rather than a singular variable such as shear stress. In the cases studied here, it was seen that the yield surfaces are essentially τ_{yy}=constant planes, with a parabolic τ_{xx} and τ_{xy} dependence at a given solid volume fraction. The role of normal stress components (τ_{yy} in particular) on yielding becomes more and more important as the suspension becomes denser, a critical aspect ignored by continuum formulations. This observation has also been made in Ref. [28].

It was seen, for the first time to our knowledge, that the stress components in the flowing suspensions display diverse dependencies with respect to length scales. While τ_{xx} and τ_{xy} depend on macroscopic parameters such as the applied pressure gradient, the transverse normal stress component, τ_{yy}, is independent of the driving force and depends only on particle-level parameters such as solid loading and wall topology. This collective behavior of the stress components explains the nondependence of shear layer thickness on driving force. The behavior of characteristic values of these stress components (wall shear stress, for example) w.r.t. plug velocity have been presented that can be possibly used for practical design. The dependence of wall shear stress on plug velocity revealed by this analysis agrees with the empirical relationship used in practice, the Benbow-Bridgewater (BB) model [5]. This shows that this modeling methodology can be potentially used to explain the physics behind the scores of empirical relationships used in the practice of extrusion flow [1,5]. This happens to be one of the motivations behind this work.

The effect of wall topology was quantitatively seen using this model. Nonplanar topologies (sinusoid, sawtooth and square well) with topological dimensions of the same order of magnitude as the particle diameter have a strong effect on the flow velocities. A reduction in plug velocity of around 60% from the planar wall case was seen. Also, appreciable differences in velocities among the three wall topologies of the same amplitude and wavelength were seen with the sinusoidal topology consistently yielding the lowest velocity. This observation is unforeseen. An inspection of the stress components revealed that the sinusoidal wall provides the most compaction to the flowing suspension. The fundamental reason behind this needs to be investigated further.

The insights presented here display that in dense suspensions, both the system-level parameters and particle-level parameters have strong effects on their flow and deformation, and controlling them should entail consideration of the two length scales on equal footing. The strong effect of wall-topology reported here, in particular, strengthens this argument.

Finally, a few words about the veracity of the new findings of this work are due. We believe that the findings are accurate because the basic methodology used is well-tested and validated, both by the authors and in other works as reported in the paper. The computer code, LAMMPS, used is a well-tested and versatile tool. The validations presented in this work specific to this problem further adds strength to the cause. Most importantly, the analyses presented comprehensively explain the observed phenomena, both specific and general, in the experimental works referenced in the text. Also, some of the relationships derived using this model, such as the one between shear stress and plug velocity in Sec. III, agrees with the experimentally based empirical correlations used in practice.

The modeling paradigm presented here can be used to study many other aspects of suspension flows, some of them

being: the effect of polydispersity on yielding, the effect of solid-solid interactions on flow behavior and yielding, and the effect of particle shape. Understanding all of these aspects will significantly enhance our understanding of suspension flows. The methodology presented here and the insights reported, it is hoped, will be a step in this direction.

[1] D. I. Wilson and S. L. Rough, Chem. Eng. Sci. **61**, 4147 (2006).
[2] L. Isa, R. Besseling, and W. C. K. Poon, Phys. Rev. Lett. **98**, 198305 (2007).
[3] P. R. Nott and J. F. Brady, J. Fluid Mech. **275**, 157 (1994).
[4] Ronald J. Phillips, R. C. Armstrong, and Robert A. Brown, Phys. Fluids A **4**, 30 (1992).
[5] John Benbow and John Bridgewater, *Paste Flow and Extrusion* (Clarendon Press, Oxford, 1993).
[6] D. Bonn and M. M. Denn, Science **324**, 1401 (2009).
[7] Y. Yan, Z. Zhang, D. Cheneler, J. R. Stokes, and M. J. Adams, Rheol. Acta **49**, 255 (2010).
[8] P. J. Hoogerbrugge and J. M. V. A. Koelman, EPL **19**, 155 (1992).
[9] R. G. Groot and P. B. Warren, J. Chem. Phys. **107**, 4423 (1997).
[10] E. G. Flekkoy, P. V. Coveney, and G. De Fabritiis, Phys. Rev. E **62**, 2140 (2000).
[11] A. Chatterjee and L. M. Wu, Mol. Simul. **34**, 243 (2008).
[12] C. Marsh, Ph.D. thesis, University of Oxford, 1998.
[13] I. V. Pivkin and G. E. Karniadakis, J. Comput. Phys. **207**, 114 (2005).
[14] E. S. Boek, P. V. Coveney, H. N. W. Lekkerkerker, and P. van der Schoot, Phys. Rev. E **55**, 3124 (1997).
[15] M. Whittle and E. Dickinson, J. Colloid Interface Sci. **242**, 106 (2001).
[16] J. Israelachvili, *Intermolecular and Surface Forces* (Academic, New York, 2003).
[17] M. Hecht, J. Harting, T. Ihle, and H. J. Herrmann, Phys. Rev. E **72**, 011408 (2005).
[18] S. Kim and S. J. Karrila, *Microhydrodynamics: Principles and Selected Applications* (Dover, New York, 2005).
[19] A. Chatterjee, D. R. Heine, A. L. Rovelstad, and L.-M. Wu, Phys. Rev. E **80**, 021406 (2009).
[20] J. T. Padding and A. A. Louis, Phys. Rev. E **74**, 031402 (2006).
[21] Y. Yan and J. Koplik, Phys. Fluids **21**, 013301 (2009).
[22] S. J. Plimpton, J. Comput. Phys. **117**, 1 (1995).
[23] P. J. in't Veld, M. K. Petersen, and G. S. Grest, Phys. Rev. E **79**, 021401 (2009).
[24] G. S. Grest, P. J. in 't Veld, and J. B. Lechman, AIP Conf. Proc. **982**, 304 (2008).
[25] O. Pouliquen and R. Gutfraind, Phys. Rev. E **53**, 552 (1996).
[26] M. P. Allen and D. J. Tildesley, *Computer Simulation of Liquids* (Oxford University Press, New York, 1987).
[27] P. Jop, Y. Forterre, and O. Pouliquen, Nature (London) **441**, 727 (2006).
[28] A. Fall, F. Bertrand, G. Ovarlez, and D. Bonn, Phys. Rev. Lett. **103**, 178301 (2009).
[29] A. J. Liu and S. R. Nagel, Nature (London) **396**, 21 (1998).
[30] H. W. Chandler, S. D. George, and J. Liddle, Br. Ceram. Trans. **101**, 47 (2002).